

Exciton g -factors in monolayer and bilayer WSe_2 from experiment and theory

Jonathan Förste,¹ Nikita V. Tepliakov,^{2,3} Stanislav Yu. Kruchinin,⁴ Jessica Lindlau,¹ Victor Funk,¹ Michael Förg,¹ Kenji Watanabe,⁵ Takashi Taniguchi,⁵ Anvar S. Baimuratov,¹ and Alexander Högele^{1,6}

¹*Fakultät für Physik, Munich Quantum Center, and Center for NanoScience (CeNS), Ludwig-Maximilians-Universität München, Geschwister-Scholl-Platz 1, D-80539 München, Germany*

²*Chair of Computational Condensed Matter Physics (C3MP), Institute of Physics,*

Ecole Polytechnique Fédérale de Lausanne (EPFL), CH-1015 Lausanne, Switzerland

³*Information Optical Technologies Center, ITMO University, 197101 Saint Petersburg, Russia*

⁴*Center for Computational Materials Sciences, Faculty of Physics, University of Vienna, Sensengasse 8/12, A-1090 Vienna, Austria*

⁵*National Institute for Materials Science, Tsukuba, Ibaraki 305-0044, Japan*

⁶*Munich Center for Quantum Science and Technology (MCQST), Schellingtr. 4, D-80799 München, Germany*

(Dated: March 5, 2020)

The optical properties of monolayer and bilayer transition metal dichalcogenide semiconductors are governed by excitons in different spin and valley configurations, providing versatile aspects for van der Waals heterostructures and devices. We present experimental and theoretical studies of exciton energy splittings in external magnetic field in neutral and charged WSe_2 monolayer and bilayer crystals embedded in a field effect device for active doping control. We develop theoretical methods to calculate the exciton g -factors from first principles and tight-binding for all possible spin-valley configurations of excitons in monolayer and bilayer WSe_2 including valley-indirect exciton configurations. Our theoretical and experimental findings shed light on some of the characteristic photoluminescence peaks observed for monolayer and bilayer WSe_2 . In more general terms, the theoretical aspects of our work provide new guidelines for the characterization of single and few-layer transition metal dichalcogenides, as well as their heterostructures, in the presence of external magnetic fields.

I. INTRODUCTION

Monolayer (ML) and bilayer (BL) transition metal dichalcogenides (TMDs) such as WSe_2 represent semiconductor building blocks for novel van der Waals heterostructures. By virtue of sizable light-matter coupling governed by excitons [1] they exhibit versatile potential for applications in photonics and optoelectronics [2, 3], opto-valleytronics [4, 5] and polaritonics [6]. Most recently, the optical interface to TMDs has been instrumental for the observation of strongly correlated electron phenomena in twisted homo- and heterobilayer moiré systems [7–9].

The key to further developments of van der Waals heterostructures for fundamental studies and practical devices using TMD MLs and BLs is the detailed understanding of their optical properties. While substantial understanding of zero-momentum excitons in ML and BL WSe_2 has been established [1], some important aspects remain subject of debate [10]. This holds, in particular, for valley-dark excitons with finite center-of-mass momentum that escape direct optical probes by virtue of momentum mismatch with photons. In MLs, they complement the notion of intravalley spin-bright and spin-dark excitons [1], and they entirely dominate the photoluminescence (PL) from the lowest-energy states in native homobilayers of WSe_2 [11].

Within the realm of optical spectroscopy techniques, magneto-spectroscopy provides means for studying the exciton spin and valley degrees of freedom. Magneto-luminescence experiments on ML WSe_2 in the presence of out-of-plane and in-plane magnetic fields, for instance, have been used to quantify the valley Zeeman splitting of bright excitons [12–17], or to brighten spin-dark excitons [18–20], respectively. To date, however, a rigorous assignment of exciton g -factors to inter-

valley excitons with finite momentum falls short mainly due to the lack of theoretical predictions [10].

In this work, we develop theoretical methods to evaluate g -factors for excitons in different spin and valley configurations, and provide explicit values for WSe_2 ML and BL excitons composed from electron and hole states away from high symmetry points of the first Brillouin zone. Our calculations go beyond the existing tight-binding (TB) models by employing the density functional theory (DFT). We compare our theoretical results with experimentally determined g -factors of intravalley excitons, and use them to interpret ambiguous peaks in the PL spectra of ML and BL WSe_2 attributed to intervalley excitons.

II. EXPERIMENTAL RESULTS

In our experiments we used a field-effect heterostructure based on an exfoliated WSe_2 crystal with extended ML and BL regions that was encapsulated in hexagonal boron nitride (hBN). The device layout is shown schematically in Fig. 1(a), and the first Brillouin zone of ML and BL WSe_2 with most relevant points in Fig. 1(b). To control the charge doping level, the crystal was contacted by a gold electrode deposited on a 50 nm thick thermal silicon oxide layer of a highly p-doped silicon substrate. With the electrode grounded, a voltage applied to the doped silicon back gate was used to control the doping in both ML and BL regions. The sample was mounted in a cryogenic confocal microscope and cooled down in a closed-cycle magneto-cryostat with a base temperature of 3.2 K. The PL was excited with a continuous-wave laser diode at 1.85 eV focussed to the diffraction-limited confocal excitation and detection spots of a low-temperature apochromatic objective, dispersed with a monochromator and detected with

a nitrogen-cooled CCD. The excitation power of a few μW was kept below the regimes of neutral and charged biexcitons [21–24]. Magneto-luminescence experiments were performed in Faraday configuration with a bi-directional solenoid at magnetic fields of up to 9 T.

The evolution of the PL with the gate voltage is shown in Fig. 1(c) and (d) for representative spots of ML and BL regions, respectively. In Fig. 1(c), the ML reaches the intrinsic limit at gate voltages below -5 V consistent with residual n-doping of the exfoliated crystal [25, 26]. The neutral regime is characterized by the bright exciton PL (X^0) at 1.72 eV and a series of red-shifted peaks that we label as M_1^0 , M_2^0 and M_3^0 . None of these peaks with respective red-shifts of 35, 60 and 75 meV from the bright exciton peak is to be attributed to the PL of dark excitons (D^0) with 42 meV red-shift [20, 27, 28]. In our sample, this feature is a rather weak shoulder at the low-energy side of M_1^0 . At positive gate voltages, the ML is charged with electrons and thus exhibits the characteristic signatures of a bright trion doublet (X_1^- and X_2^-) split by the exchange energy of ~ 6 meV [26], the dark trion (D^-) at 28 meV red-shift from X_1^- [29–32], and a series of low-energy peaks dominated by the peak M_1^- at 44 meV red-shift [31, 32].

The PL from the BL region in Fig. 1(d) is characterized by a multi-peak structure, more than 100 meV below X^0 . It exhibits the same limits of charge neutrality and electron doping as a function of the gate voltage, consistent with the charging behavior of the ML in Fig. 1(c). The BL peaks, labelled by an increasing subscript number with decreasing peak energy as B_1^0 through B_3^0 and B_1^- through B_3^- in the neutral and negative regime, respectively, correspond to phonon-sidebands of neutral and charged momentum-indirect excitons with a global red-shift of 22 meV at about -7 V in Fig. 1(d) [11]. According to the single-particle band structure of BL WSe₂ [33, 34], the field-induced electron concentration is accommodated at the conduction band edge by the six inequivalent Q -valleys. However, the nature of the hole states that constitute the lowest-energy momentum-dark excitons as long-lived reservoirs of phonon-assisted PL remains ambiguous. The energetic proximity of the valance band edge states at K and Γ in BL WSe₂ [35] renders QK and $Q\Gamma$ excitons and trions (composed from electrons at Q and holes at K or Γ) nearly degenerate, which in turn complicates their energetic ordering [11].

To examine the origin of the BL peaks, and to shed light on the nature of ML peaks with ambiguous or partly controversial interpretation, we performed magneto-spectroscopy in the two well-defined limits of charge neutrality and negative doping. The external magnetic field B was applied along the z -axis perpendicular to the sample. It removes the valley degeneracy and splits the exciton reservoirs by their characteristic Zeeman energies proportional to the exciton g -factor in WSe₂ [12–17]. The respective polarization-contrasting spectra recorded at -8 T under linearly polarized excitation (π) and circularly polarized detection (σ^+ and σ^-) for the neutral (negatively charged) ML and BL are shown in the top (bottom) panel of Fig. 2(a) and (b).

At each magnetic field, we quantified the experimental Zeeman splitting for every PL peak as the energy difference $\Delta = E^+ - E^-$ between the peak energies E^+ and E^- recorded

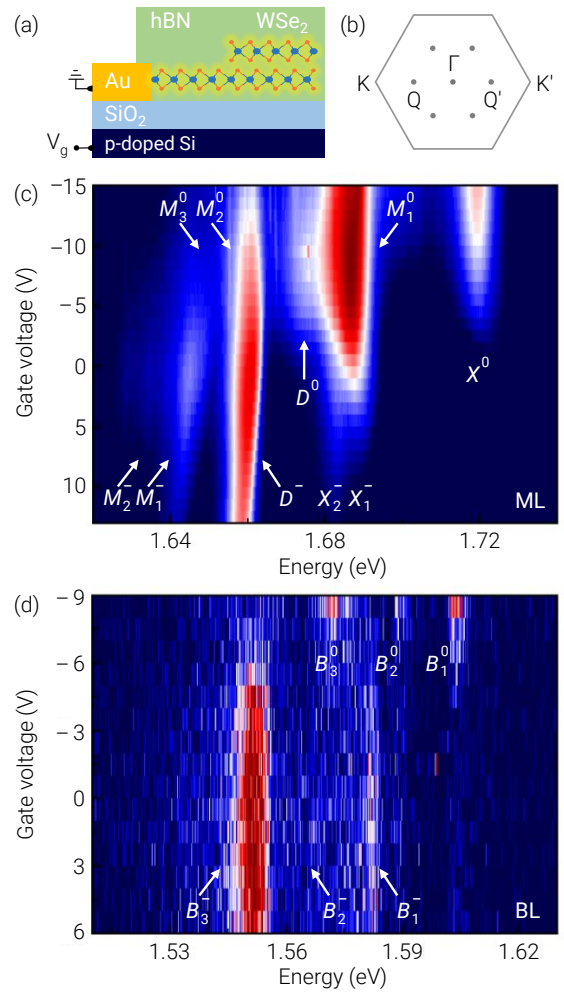


FIG. 1. Logarithmic false-color plots of the photoluminescence as a function of the gate voltage, recorded at representative positions of (a) monolayer and (b) bilayer WSe₂ regions of the same field-effect device under laser excitation at 1.85 eV. The upper and lower dashed lines indicate the regimes of charge neutrality and negative doping, respectively, with the corresponding magneto-luminescence spectra shown in Fig. 2. The monolayer exhibits characteristic photoluminescence peaks of neutral bright (X^0) and dark (D^0) excitons as well as the negatively charged bright trion doublet (X_1^- and X_2^-) and dark trion (D^-) emission peaks. All other peaks of monolayer (M) and bilayer (B) photoluminescence are labelled according to their charge state in the superscript and an increasing subscript number.

under σ^+ and σ^- polarized detection. The left and right panels of Fig. 3(a) and (b) show Δ as a function of the magnetic field for all peaks of the neutral and negatively charged ML and BL, respectively. The set of data derived from magneto-PL measurements was complemented for X^0 , X_1^- , and X_2^- by performing magneto-reflectivity under circular excitation and detection. The corresponding experimental exciton g -factors, obtained from $\Delta = g\mu_B B$ as the slopes of best linear fits to the data in Fig. 3 scaled by the Bohr magneton μ_B , are summarized in Tab. I. The negative sign of the g -factors reflects the energy ordering of exciton states that exhibit higher (lower) energy for σ^- (σ^+) polarized PL peaks at positive magnetic

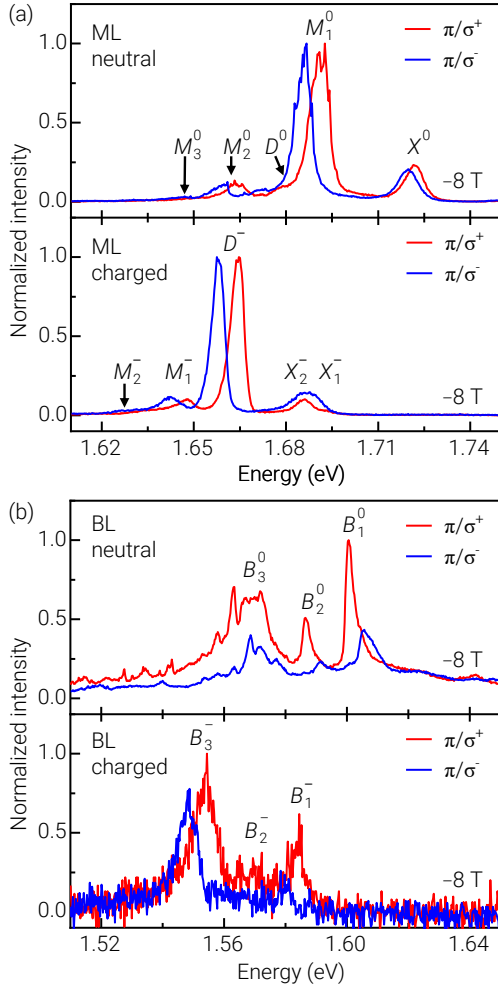


FIG. 2. Photoluminescence spectra of (a) monolayer and (b) bilayer WSe₂ in a perpendicular magnetic field of -8 T. The neutral and negatively charged regimes are shown in the top and bottom panels, respectively. The spectra were recorded with linearly polarized excitation (π) and circularly polarized detection (σ^+ and σ^-).

fields.

In ML WSe₂, the g -factors of both neutral and negatively charged excitons with the corresponding PL peaks X^0 , D^0 , X_1^- , X_2^- and D^- have been established in previous experiments on a wide range of different samples [12–20, 29–32]. Our results for the bright exciton and the trion doublet in Tab. I agree well with these reports if we discard the magneto-luminescence result for X_1^- that is compromised by both a vanishingly small PL intensity at high magnetic fields and the relatively broad linewidth of 6 meV in our sample. Due to this inhomogeneous broadening we are unable to track the dispersion of the relatively weak spin-dark exciton peak D^0 , with g -factors ranging between 9.1 and 9.9 in previous reports [20, 29, 31, 32] nor its chiral-phonon replicum with the same g -factor at 65 meV red-shift from X^0 [31, 32, 36]. The signature of the latter is overwhelmed in our spectra by the peak M_2^0 with 60 meV red-shift and a g -factor of -12.9 ± 0.7 in agreement with values

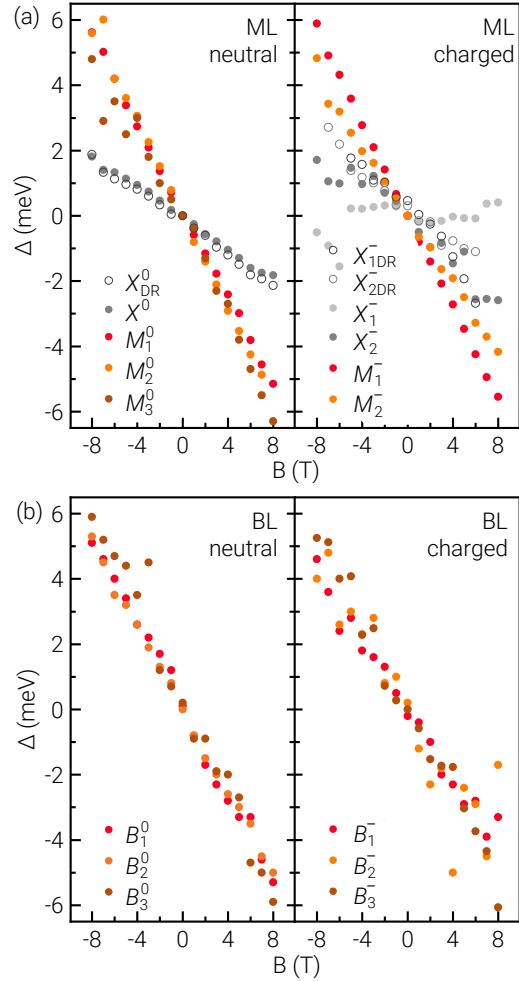


FIG. 3. Valley Zeeman splitting ΔE as a function of the magnetic field for the photoluminescence peaks (closed circles) of (a) monolayer and (b) bilayer WSe₂ in the neutral (left panel) and negatively charged (right panel) regimes, respectively. Complementary data (open circles) are from polarization-resolved reflectivity.

reported from samples with spectrally narrow PL [31, 32]. The red-most peak M_3^0 features the same g -factor within the experimental error bars as M_1^0 , suggesting a joint reservoir as their origin. The negatively charged trion D^- was reported to have the same g -factor as its neutral counterpart [29–32], whereas we determine -12.2 ± 0.1 . The agreement with previous reports is better for the peak M_1^- with a g -factor of -9.0 ± 0.1 that is supposed to be a phonon sideband of D^- [31, 32]. The latter studies also reported an intense PL peak between M_1^- and D^- with a remarkably small g -factor of -4.1 [31] and -3.4 [32]. This peak of unidentified origin is missing in our spectra from the negative doping regime.

There are other peaks in ML WSe₂ without conclusive assignment, and in particular M_1^0 has received controversial interpretation as phonon-assisted PL from virtual trions [37], phonon sidebands of momentum-dark Q -excitons [38], or zero-phonon PL of finite-momentum excitons in spin-like con-

TABLE I. Experimental g -factors obtained from magneto-luminescence (^acomplementary data from magneto-reflectivity) of neutral and negatively charged monolayer and bilayer WSe₂.

ML				BL		
X^0	M_1^0	M_2^0	M_3^0	B_1^0	B_2^0	B_3^0
-4.1	-11.5	-12.6	-11.4	-11.4	-10.8	-12.8
± 0.1	± 0.1	± 0.2	± 0.4	± 0.2	± 0.1	± 0.2
X_1^-	X_2^-	D^-	M_1^-	B_1^-	B_2^-	B_3^-
-4.6	-1.3	-12.2	-9.0	-9.1	-9.8	-11.5
± 0.3	± 0.3	± 0.1	± 0.1	± 0.3	± 1.0	± 0.4

^a X^0 : -4.3 ± 0.1 ; X_1^- : -4.7 ± 0.3 ; X_2^- : -6.5 ± 0.4

figuration [32] that we denote as K'_L . Due to the lack of theory for the g -factors of excitons with finite center-of-mass momentum, the task of confronting the competing hypotheses with the characteristic valley Zeeman splittings of controversial ML peaks has remained elusive. The same shortcoming holds for both neutral and charged BL excitons with finite center-of-mass momentum. To shed additional light on the nature of PL peaks in both ML and BL WSe₂, we calculate in the following the g -factors for excitons in different spin and valley configurations from TB and DFT.

III. THEORETICAL FORMALISM

We consider a crystal electron in a Bloch state $\psi_{n\mathbf{k}}(\mathbf{r}) = S^{-1/2} \exp(i\mathbf{k}\mathbf{r})u_{n\mathbf{k}}(\mathbf{r})$ with energy $E_{n\mathbf{k}}$, where n is the band number, \mathbf{k} is the wave vector, $u_{n\mathbf{k}}(\mathbf{r})$ is the periodic Bloch amplitude, and S is the normalization area. In the presence of a weak perturbation by a static magnetic field \mathbf{B} , the first-order correction to the electron energy is proportional to \mathbf{B} and given by [41]:

$$V_n(\mathbf{k}) = \mu_B \mathbf{B} [g_0 \mathbf{s} + \mathbf{L}_n(\mathbf{k})], \quad (1)$$

where $\mu_B = |e|\hbar/(2m_0c)$ is the Bohr magneton, e and m_0 are the charge and mass of the free electron, and c is the speed of light. The expression in square brackets is usually called the effective magnetic moment [42, 43], which contains both spin and orbital contributions. In particular the first term is proportional to the free electron Landé factor $g_0 \simeq 2$ and the spin angular momentum $\mathbf{s} = \sigma/2$, where σ denotes the Pauli matrix.

The second term, $\mathbf{L}_n(\mathbf{k}) = \langle \psi_{n\mathbf{k}}(\mathbf{r}) | \mathbf{L} | \psi_{m\mathbf{k}}(\mathbf{r}) \rangle$, is the orbital angular momentum with the operator $\mathbf{L} = \hbar^{-1}[\mathbf{r} \times \mathbf{p}]$. To obtain its matrix elements one can reduce the calculation to the interband matrix elements of the momentum operator \mathbf{p} or the operator of the space coordinate \mathbf{r} [14, 42–44]:

$$\mathbf{L}_n(\mathbf{k}) = \frac{1}{im_0} \sum_{m \neq n} \frac{[\mathbf{p}_{nm}(\mathbf{k}) \times \mathbf{p}_{mn}(\mathbf{k})]}{E_{n\mathbf{k}} - E_{m\mathbf{k}}}, \quad (2)$$

$$\mathbf{L}_n(\mathbf{k}) = \frac{m_0}{i\hbar^2} \sum_{m \neq n} [\xi_{nm}(\mathbf{k}) \times \xi_{mn}(\mathbf{k})] (E_{n\mathbf{k}} - E_{m\mathbf{k}}), \quad (3)$$

where m is the sum over all bands but the band of interest, and $\xi_{nm}(\mathbf{k}) = i \langle u_{n\mathbf{k}}(\mathbf{r}) | \partial/\partial \mathbf{k} | u_{m\mathbf{k}}(\mathbf{r}) \rangle$ is the interband matrix element of the crystal coordinate operator.

In the following, we restrict our analysis to the orientation of the magnetic field along the z -axis and define the electron Zeeman splitting as the difference between the energy of the electron state with wave vector $+\mathbf{k}$ and spin projection $+s$ along the z -axis and the state with $-\mathbf{k}$ and $-s$ as:

$$\Delta_n(\mathbf{k}) = V_n(+\mathbf{k}) - V_n(-\mathbf{k}) = 2\mu_B B [g_0 s + L_n(\mathbf{k})]. \quad (4)$$

Thus, the electron g -factor of Bloch electrons in the n -th band can be written as:

$$g_n(\mathbf{k}) = \frac{\Delta_n(\mathbf{k})}{\mu_B B} = \pm g_0 + 2L_n(\mathbf{k}) \quad (5)$$

with $+$ ($-$) for $s = +1/2$ ($-1/2$) corresponding to spin up (down) projections along z denoted as \uparrow (\downarrow), and the explicit expression for the z -component of the orbital angular momentum:

$$L_n(\mathbf{k}) = \frac{2}{m_0} \sum_{m \neq n} \frac{\text{Im} \left[\rho_{nm}^{(x)}(\mathbf{k}) \rho_{mn}^{(y)}(\mathbf{k}) \right]}{E_{n\mathbf{k}} - E_{m\mathbf{k}}}, \quad (6)$$

$$L_n(\mathbf{k}) = \frac{2m_0}{\hbar^2} \sum_{m \neq n} \text{Im} \left[\xi_{nm}^{(x)}(\mathbf{k}) \xi_{mn}^{(y)}(\mathbf{k}) \right] (E_{n\mathbf{k}} - E_{m\mathbf{k}}). \quad (7)$$

To calculate the contributions of the conduction (c) band electron with \mathbf{k}_c, s_c and the hole (h) with \mathbf{k}_h, s_h to the exciton g -factor, we neglect electron-hole Coulomb interactions [14]. In this case, the exciton Zeeman splitting simplifies to the sum of the Zeeman splittings of the electron and the hole. Using time reversal symmetry which relates the spin and wave vector of the hole to the corresponding spin and wave vector of the empty electron state in the valence (v) band ($s_h = -s_v$ and $\mathbf{k}_h = -\mathbf{k}_v$), we obtain the exciton g -factor as

$$g^{(cv)}(\mathbf{k}_c, \mathbf{k}_v) = g_c(\mathbf{k}_c) - g_v(\mathbf{k}_v). \quad (8)$$

Finally, by reference to the valence band electron with $\mathbf{k}_v = K$ or Γ with spin-up projection $s_v = +1/2$, we discriminate spin-like (L) excitons (with $s_c = s_v$) from spin-unlike (U) excitons (with $s_c = -s_v$). Their respective exciton g -factors are given by:

$$g_L^{(cv)}(\mathbf{k}_c, \mathbf{k}_v) = 2[L_c(\mathbf{k}_c) - L_v(\mathbf{k}_v)], \quad (9)$$

$$g_U^{(cv)}(\mathbf{k}_c, \mathbf{k}_v) = 2[L_c(\mathbf{k}_c) - L_v(\mathbf{k}_v)] - 2g_0. \quad (10)$$

Using these expressions, we evaluate in the following the exciton g -factors from the matrix elements of the orbital angular momentum, $L_c(\mathbf{k}_c)$ and $L_v(\mathbf{k}_v)$, obtained within TB and DFT calculations.

IV. TIGHT-BINDING APPROXIMATION

We begin by calculating the g -factors of excitons in both spin-like and spin-unlike configurations of states from different

TABLE II. Two sets of tight-binding fitting parameters for monolayer WSe₂: TB-1 from Ref. 39 and TB-2 from Ref. 40 (in units of eV).

Set	$t_{6,6}^{(1)}$	$t_{7,7}^{(1)}$	$t_{8,8}^{(1)}$	$t_{6,7}^{(1)}$	$t_{6,8}^{(1)}$	$t_{7,8}^{(1)}$	$t_{9,9}^{(1)}$	$t_{10,10}^{(1)}$	$t_{11,11}^{(1)}$	$t_{9,10}^{(1)}$	$t_{9,11}^{(1)}$	$t_{10,11}^{(1)}$		
	$t_{9,6}^{(5)}$	$t_{11,6}^{(5)}$	$t_{10,7}^{(5)}$	$t_{9,8}^{(5)}$	$t_{11,8}^{(5)}$	$t_{9,6}^{(6)}$	$t_{11,6}^{(6)}$	$t_{9,8}^{(6)}$	$t_{11,8}^{(6)}$	ϵ_6	$\epsilon_{7,8}$	ϵ_9	$\epsilon_{10,11}$	
TB-1	-0.3330	0.3190	-0.5837	-0.1250	0.4233	-0.2456	-0.2399	1.0470	0.0029	0.1857	-0.0377	-0.1027		
	-0.8998	-0.9044	1.4030	-0.8548	0.5711	-0.0676	-0.1608	-0.2618	-0.2424	-0.1667	0.0984	-3.3642	-2.1820	
TB-2	-0.985	0.618	-0.775	-0.853	-0.0083	-0.412	0.191	1.22	0.028	-0.176	-0.039	-0.228		
	-0.8	0.183	1.8	0.811	-0.0766	0.993	0.728	0.888	0.31	-0.999	-0.047	-1.69	-2.25	

conduction and valence band valleys according to Eq. 9 and 10 using the results of the eleven-band and six-band TB models of Ref. 39 and Ref. 40. Without taking into account spin-orbit interactions, we evaluate the matrix elements $L_c(\mathbf{k}_c)$ and $L_v(\mathbf{k}_v)$ for the doubly degenerate states of the conduction band at K and Q and the valence band at K and Γ . By symmetry, the ML energy bands can be classified as odd or even with respect to their reflection in the plane. In the following, we restrict ourselves to even bands with finite contributions to the g -factors of excitons with lowest energies [40] and use the notations for orbital indices and hopping integrals from the TB model of Fang *et al.* [39].

In WSe₂ ML, the relevant even bands are formed by even d -orbitals of W atoms ($\varphi_6 = d_{z^2}$, $\varphi_7 = d_{xy}$, and $\varphi_8 = d_{x^2-y^2}$) and Se dimers (which include the anti-symmetric combination $\varphi_9 = (p_z^A - p_z^B)/\sqrt{2}$ as well as two symmetric combinations $\varphi_{10} = (p_x^A + p_x^B)/\sqrt{2}$ and $\varphi_{11} = (p_y^A + p_y^B)/\sqrt{2}$ of p -orbitals of Se). The electron Bloch state within the six-band TB model is approximated as a linear combination of atomic orbitals as [40]:

$$\psi_{n\mathbf{k}}(\mathbf{r}) = \sum_{j,l} e^{i\mathbf{k}\mathbf{a}_{jl}} c_{nl}(\mathbf{k}) \varphi_l(\mathbf{r} - \mathbf{a}_{jl}), \quad (11)$$

where j runs over all unit cells, $l = 6 - 11$ enumerates the six even orbitals, and the vectors $\mathbf{a}_{j,6} = \mathbf{a}_{j,7} = \mathbf{a}_{j,8}$ and $\mathbf{a}_{j,9} = \mathbf{a}_{j,10} = \mathbf{a}_{j,11}$ point to the positions of W and Se atoms in the j -th unit cell.

The TB Hamiltonian for the even energy bands is given by a 6×6 matrix of the form:

$$H_{ll'}(\mathbf{k}) = \begin{pmatrix} H_{W-W} & H_{W-Se}^\dagger \\ H_{W-Se} & H_{Se-Se} \end{pmatrix}, \quad (12)$$

where the 3×3 matrices H_{W-W} , H_{Se-Se} , and H_{W-Se} describe the interactions between W-W, Se-Se, and Se-W atoms, respectively.

According to Ref. 39, the six-band TB Hamiltonian has 25 independent fitting parameters: two sets of six hopping integrals $t_{l,l'}^{(1)}$ between the first-neighbor pairs (each for W-W and Se-Se), five parameters $t_{l,l'}^{(5)}$ and four parameters $t_{l,l'}^{(6)}$ for the first- and second-neighbor pairs of atoms of different kinds, and four on-site energies $\epsilon_6, \epsilon_{7,8}, \epsilon_9, \epsilon_{10,11}$.

With two sets of parameters reproduced from the original work of Ref. 39 (TB-1) and Ref. 40 (TB-2) for ML WSe₂ in Tab. II, we calculate the matrix elements of the orbital

angular momentum using Eq. (6) and the matrix elements of the momentum operator [45, 46]

$$\mathbf{p}_{nm}(\mathbf{k}) = \frac{m_0}{\hbar} \sum_{l,l'} c_{nl}^*(\mathbf{k}) c_{ml'}(\mathbf{k}) \frac{\partial H_{ll'}(\mathbf{k})}{\partial \mathbf{k}}. \quad (13)$$

Fig. 5 (a) and (b) show the values of $L_n(\mathbf{k})$ within the first Brillouin zone evaluated according to Eq. (6) for the highest valence band (left panels) and the lowest conduction band (right panels) with the set of parameters from the models TB-1 and TB-2, respectively. The g -factors of excitons in specific spin and valley configurations calculated with in Eqs. (9) and (10) are listed in Tab. III.

V. DENSITY FUNCTIONAL THEORY

DFT provides a complementary approach to the calculation of exciton g -factors by yielding the energy band structure $E_{n\mathbf{k}}$ and the matrix elements $\xi_{nm}(\mathbf{k})$. The angular momenta $L_c(\mathbf{k}_c)$ and $L_v(\mathbf{k}_v)$ are obtained from Eq. (7), and the exciton g -factors follow from Eqs. (9) and (10). Our DFT calculations were carried out for ML and BL WSe₂ within the generalized gradient approximation (GGA). In brief, the first-principles calculations were performed with the PBEsol exchange-correlation functional [47] as implemented in the Vienna *ab initio* simulation package (VASP). The van der Waals interactions were considered with the DFT-D3 method with Becke-Johnson damping [48, 49]. The spin-orbit interaction was included at all stages. Elementary cells with a vacuum thickness of 35 Å were used in order to minimize interactions between periodic images. The atomic positions were relaxed with a cut-off energy of 400 eV until the change in the total energy was less than 10^{-6} eV. The band structure of ML (BL) was calculated on the Γ -centered \mathbf{k} grid of 36×36 (18×18) divisions with 80 (160) bands.

In Fig. 4(a) and (b) we show the convergence of the orbital angular momenta $L_n(\mathbf{k})$ within our ML and BL calculations as a function of the number of bands taken into account in the sum of Eq. (7). For the ML, Fig. 4(a) shows the results for the top-most valence band state v at K (blue solid line), the two highest valence band states v and $v - 1$ at Γ (grey solid and dashed lines), as well as the two lowest conduction band states c and $c + 1$ at K and Q (red and black solid and dashed lines). As the BL bands are doubly degenerate, each \mathbf{k} -point of the Brillouin zone has at least two bands with $L_n(\mathbf{k}) = L_{n+1}(\mathbf{k})$

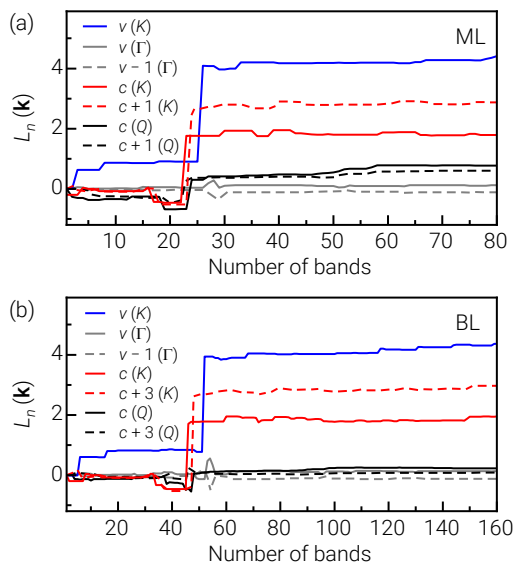


FIG. 4. Convergence of the electron orbital angular momentum in DFT calculations for the highest valence bands at K and Γ and the lowest conduction bands at K and Q in (a) monolayer and (b) bilayer WSe_2 .

or $L_n(\mathbf{k}) = L_{n-1}(\mathbf{k})$. For the BL in Fig. 4(b) we consider the same \mathbf{k} -points as for the ML, and show the corresponding bands where the orbital angular momenta have the same sign as in the ML case of Fig. 4(a).

For the orbital angular momenta of these states, convergence is observed above 60 and 120 bands in the case of ML and BL in Fig. 4(a) and (b), respectively, with the factor of two difference related to the doubled number of atoms in BL calculations. We note that the values for the valence band states at Γ must vanish by symmetry arguments, whereas our numerical calculations yield ± 0.12 for both ML and BL. This discrepancy is due to a finite number of bands taken into account and can be used to estimate the precision of our numerical calculations. The corresponding bound on the absolute error of the exciton g -factors from DFT, given explicitly in Tab. III for selected exciton configurations, is thus in the order of ± 0.5 .

As for the TB calculations, we plot in Fig. 5(c) the DFT results for $L_n(\mathbf{k})$ within the first Brillouin zone. Since spin-orbit effects were included at the DFT level, it is instructive to show both spin-orbit split highest valence bands (v and $v-1$) and lowest conduction bands (c and $c+1$). All models agree with respect to the sign, and at least qualitatively, in the overall dependence of $L_v(\mathbf{k})$ in the valence bands (left panel). A qualitative agreement between TB-1 and DFT is also apparent for the conduction bands (right panel) in striking contrast to the results of TB-2 that predicts reversed signs for $L_c(\mathbf{k})$ throughout almost the entire Brillouin zone. The results of the model also differ substantially from TB-1 and DFT values of $L_v(\mathbf{k})$ at the quantitative level. We conclude from this comparison that the correspondence between $L_n(\mathbf{k})$ and thus between the exciton g -factors obtained from DFT and TB is sensitive to the details of the TB fitting procedures. The main shortcoming of TB models could possibly result from

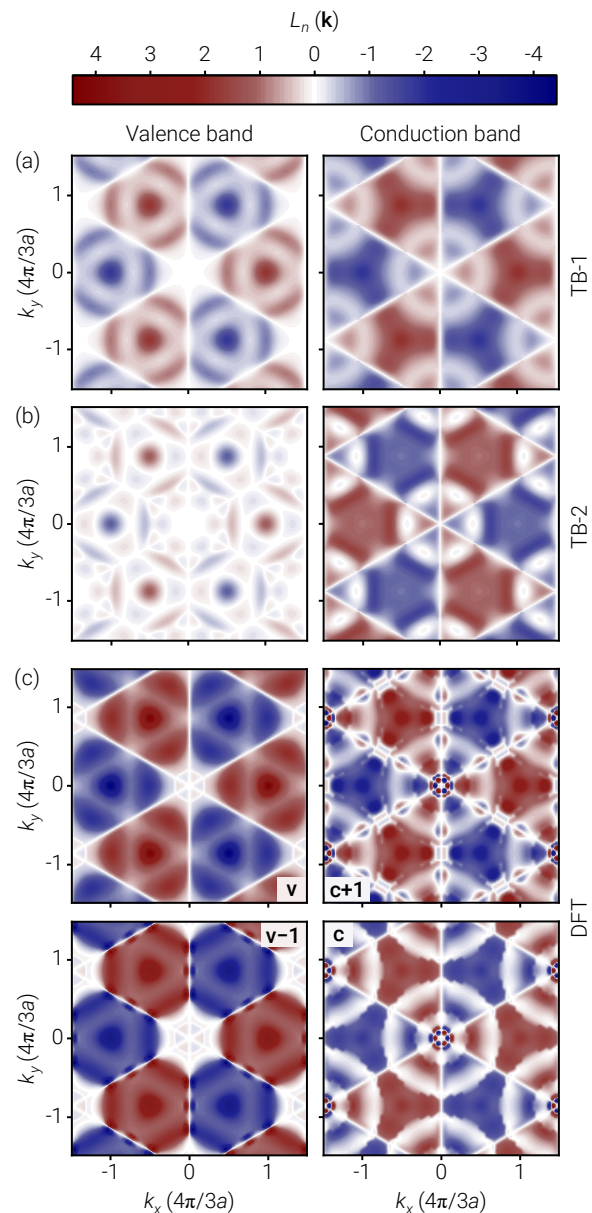


FIG. 5. Orbital angular momentum in the first Brillouin zone calculated for the top-most valence (left panels) and lowest conduction (right panels) bands from (a) TB-1, (b) TB-2 and (c) DFT. Note that the valence and conduction bands are spin-degenerate in tight-binding without spin-orbit effects, whereas the valence bands v and $v-1$ and the conduction bands c and $c+1$ are split by the respective spin-orbit splitting in DFT calculations.

the fact that they are limited to d - and p -orbitals of W and Se atoms, respectively, and neglect the contributions from other orbitals.

With the matrix elements of the orbital angular momenta of the valence and conduction bands in Fig. 5 obtained from TB and DFT for the first Brillouin zone, it is straight forward to calculate the g -factors of the lowest-energy ML excitons in various configurations. In Tab. III we compare the g -factors obtained from TB-1 and TB-2 models with our DFT results

TABLE III. Exciton g -factors calculated for ML WSe₂ from TB-1, TB-2 and DFT. The g -factors in the two right-most columns for BL WSe₂ intralayer (Intra) and interlayer (Inter) excitons are both from DFT. Note that without further assumptions the sign of the g -factor is only meaningful for zero-momentum spin-like excitons with valley-contrasting dipolar selection rules.

Exciton	Valley $\mathbf{k}_c, \mathbf{k}_v$	Spin s_c, s_v	ML			BL	
			TB-1	TB-2	DFT	Intra	Inter
X^0	KK	$\uparrow\uparrow$	0.2	-4.2	-3.1	-2.8	-12.6
D^0	KK	$\downarrow\downarrow$	3.8	8.2	9.2	8.8	18.6
K'_L	$K'K$	$\uparrow\uparrow$	7.4	0.4	12.4	12.6	2.8
K'_U	$K'K$	$\downarrow\downarrow$	11.4	4.4	18.5	18.6	8.8
Q_L	QK	$\uparrow\uparrow$	3.0	2.7	7.3	8.3	8.9
Q_U	QK	$\downarrow\downarrow$	7.0	6.7	11.6	13.1	12.6
Q'_L	$Q'K$	$\uparrow\uparrow$	4.3	1.9	10.0	8.9	8.3
Q'_U	$Q'K$	$\downarrow\downarrow$	8.3	5.9	14.4	12.6	13.1
	$K\Gamma$	$\uparrow\uparrow$	3.8	1.9	5.8	5.9	3.9
	$K\Gamma$	$\downarrow\downarrow$	0.2	5.9	0.4	0.1	9.9
	$K'\Gamma$	$\uparrow\uparrow$	3.8	1.9	3.6	3.9	5.9
	$K'\Gamma$	$\downarrow\downarrow$	7.8	2.1	9.8	9.9	0.1
	$Q\Gamma$	$\uparrow\uparrow$	0.7	0.4	1.5	0.4	0.2
	$Q\Gamma$	$\downarrow\downarrow$	3.3	4.4	2.8	3.8	4.4
	$Q'\Gamma$	$\uparrow\uparrow$	0.7	0.4	1.2	0.2	0.4
	$Q'\Gamma$	$\downarrow\downarrow$	4.7	3.6	5.5	4.4	3.8

for excitons in different configurations of valleys ($\mathbf{k}_c, \mathbf{k}_v$) and spins (s_c, s_v , with \uparrow or \downarrow projection along z).

In the top block of Tab. III, we list excitons with the hole at K and the electron at K or K' in spin-like and spin-unlike configurations with short exciton notation for zero-momentum bright and dark neutral excitons X^0 and D^0 and their finite-momentum counterparts K'_L and K'_U . The block below shows the results for the spin-like and spin-unlike Q -excitons with the electron in Q and the hole in K , followed by two blocks without short exciton notation for momentum-indirect excitons composed from electrons in K or Q and holes in Γ . Note that the sign of the g -factor can be determined without further assumptions only for X^0 with established dipolar selection rules (the D^0 emission is in-plane and linearly polarized). For Zeeman-split momentum-indirect excitons, in contrast, additional symmetry analysis is required to determine their g -factor sign from the energetic ordering and polarization of the respective phonon sidebands by taking into account the symmetry of the actual phonons involved in first or higher-order scattering processes that mediate the phonon-assisted PL [32].

VI. DISCUSSION

First, we discuss the results of our calculations for excitons in ML WSe₂. The g -factor from TB-2 is very close to the experimental value of -4 for X^0 [12–17], whereas our

DFT model predicts -3.1 , and the result from TB-1 of 0.2 is completely off. We note that the disagreement between experiment and DFT is actually surprisingly small given the sample-to-sample variations in experimental reports [12–17] and the limited number of bands included in our DFT calculations. We expect the agreement to improve with the number of bands and approach the excellent agreement in the g -factor of spin-dark excitons with $g \simeq 9.4$ in experiment [20] and 9.2 in DFT.

The states K'_L and K'_U , which are the momentum-indirect counterparts of X^0 and D^0 , respectively, exhibit different g -factors with large values of 12.4 and 18.5 not predicted by either of the two TB models. We find a similar discrepancy between large (7.3 to 14.4) and small (1.9 to 8.3) g -factor values from DFT and TB for Q -momentum excitons, whereas all theories agree on the smallness of g -factors for excitons with the hole at Γ . As expected, the g -factors of intralayer excitons in BL WSe₂ are close to the values of the corresponding ML excitons [50]. In addition to intralayer excitons, the BL hosts interlayer counterparts (*e.g.* intralayer Q_L and interlayer Q'_L , intralayer Q_U and interlayer Q'_U , an so on) that exhibit the same g -factors in our model which neglects Coulomb corrections for intralayer and interlayer excitons.

By providing explicit g -factor values for momentum-indirect excitons, our DFT results complement the experimental observations in ML and BL WSe₂. In the framework of neutral MLs, however, they do not resolve the ambiguity between the two competing explanations of the peak M_1^0 . The assignment of the peak as a phonon sideband of Q -momentum excitons [38], on the one hand, is consistent with the g -factors of 7.3 and 14.4 for Q_L and Q'_U states in Tab. III (note that Q_U and Q'_L excitons, 250 meV above degenerate Q_L and Q'_U states [51], are irrelevant in this context) and the structured peak M_1^0 in Fig. 2 with a g -factor of 11.5 . On the other hand, the interpretation of the peak as direct PL emission by momentum-dark K'_L excitons [32] is also consistent with the theoretical g -factor of 12.4 from DFT. Our DFT results also identifies $K\Gamma$ and $Q\Gamma$ with small g -factors as potential candidates to explain the bright PL peak between M_1^- and D^- in the negatively charged regime of high-quality samples with narrow spectra [31, 32].

For the neutral BL, our results help to rule out $Q\Gamma$ excitons and suggest spin-unlike interlayer QK and intralayer $Q'K$ exciton reservoirs rather than $K'\Gamma$ as a joint origin of phonon sidebands B_1^0, B_2^0 and B_3^0 [11]. Whereas a detailed assignment of the neutral BL peaks to the specific reservoirs and phonon sidebands is yet to be developed, the values of the exciton g -factors in the charged regime can be understood, as in the ML case, by regarding the additional electron in the charged complex simply as a spectator to the Zeeman effect of the neutral finite-momentum exciton reservoir.

VII. SUMMARY AND CONCLUSIONS

In summary, our work provides exciton g -factors for neutral and charged ML and BL WSe₂ from both experiment and theory. For neutral and charged ML WSe₂ it complements

previous experimental findings by theoretical calculations of the g -factors for momentum-indirect excitons in different configurations of spins and valleys. We find overall very good quantitative agreement with experiment for theoretical g -factor values obtained from first-principles calculations, whereas TB methods fail at matching the experimental values for some of the versatile exciton species in MLs. For BL WSe₂, our work adds new insight into the origin of PL peaks on the basis of theoretical g -factor values. In the broad context of research on layered semiconductors and their applications, the theoretical aspects of our work provide new guidelines for magneto-optical studies of single-layer TMDs, homo- or hetero-bilayer systems, and other realizations of TMD-based van der Waals heterostructures.

ACKNOWLEDGMENTS

The authors thank M. M. Glazov, T. Deilmann and P. Hawrylak for fruitful discussions. This research was funded by the

European Research Council (ERC) under the Grant Agreement No. 772195, the Volkswagen Foundation, and the Deutsche Forschungsgemeinschaft (DFG, German Research Foundation) under Germany's Excellence Strategy EXC-2111-390814868. S. Yu. K. acknowledges support from the Austrian Science Fund (FWF) within the Lise Meitner Project No. M 2198-N30. A. S. B. has received funding from the European Union's Framework Programme for Research and Innovation Horizon 2020 (2014–2020) under the Marie Skłodowska-Curie Grant Agreement No. 754388, and from LMU Munich's Institutional Strategy LMUexcellent within the framework of the German Excellence Initiative (No. ZUK22). A. H. acknowledges support from the Center for NanoScience (CeNS) and the LMUinnovativ project Functional Nanosystems (FuNS). Growth of hexagonal boron nitride crystals was supported by the MEXT Element Strategy Initiative to Form Core Research Center, Grant Number JPMXP0112101001 and the CREST(JPMJCR15F3), JST.

-
- [1] G. Wang, A. Chernikov, M. M. Glazov, T. F. Heinz, X. Marie, T. Amand, and B. Urbaszek, *Rev. Mod. Phys.* **90**, 3721 (2018).
- [2] Q. H. Wang, K. Kalantar-Zadeh, A. Kis, J. N. Coleman, and M. S. Strano, *Nat. Nanotechnol.* **7**, 699 (2012).
- [3] K. F. Mak and J. Shan, *Nat. Photonics* **10**, 216 (2016).
- [4] A. Neumann, J. Lindlau, L. Colombier, M. Nutz, S. Najmaei, J. Lou, A. D. Mohite, H. Yamaguchi, and A. Högele, *Nat. Nanotechnol.* **12**, 329 (2017).
- [5] J. R. Schaibley, H. Yu, G. Clark, P. Rivera, J. S. Ross, K. L. Seyler, W. Yao, and X. Xu, *Nat. Rev. Mater.* **1**, 16055 (2016).
- [6] C. Schneider, M. M. Glazov, T. Korn, S. Höfling, and B. Urbaszek, *Nat. Commun.* **9**, 2695 (2018).
- [7] Y. Tang, L. Li, T. Li, Y. Xu, S. Liu, K. Barmak, K. Watanabe, T. Taniguchi, A. H. MacDonald, J. Shan, and K. F. Mak, [arXiv:1910.08673](https://arxiv.org/abs/1910.08673) (2019).
- [8] E. C. Regan, D. Wang, C. Jin, M. I. B. Utama, B. Gao, X. Wei, S. Zhao, W. Zhao, K. Yumigeta, M. Blei, J. Carlstroem, K. Watanabe, T. Taniguchi, S. Tongay, M. Crommie, A. Zettl, and F. Wang, [arXiv:1910.09047 \[cond-mat\]](https://arxiv.org/abs/1910.09047) (2019).
- [9] Y. Shimazaki, I. Schwartz, K. Watanabe, T. Taniguchi, M. Kroner, and A. Imamoğlu, [arXiv:1910.13322](https://arxiv.org/abs/1910.13322) (2019).
- [10] M. Koperski, M. R. Molas, A. Arora, K. Nogajewski, A. O. Slobodeniuk, C. Faugeras, and M. Potemski, *Nanophotonics* **6**, 1289 (2017).
- [11] J. Lindlau, M. Selig, A. Neumann, L. Colombier, J. Förste, V. Funk, M. Förg, J. Kim, G. Berghäuser, T. Taniguchi, K. Watanabe, F. Wang, E. Malic, and A. Högele, *Nat. Commun.* **9**, 2586 (2018).
- [12] A. Srivastava, M. Sidler, A. V. Allain, D. S. Lembke, A. Kis, and A. Imamoğlu, *Nat. Phys.* **11**, 141 (2015).
- [13] G. Aivazian, Z. Gong, A. M. Jones, R.-L. Chu, J. Yan, D. G. Mandrus, C. Zhang, D. Cobden, W. Yao, and X. Xu, *Nat. Phys.* **11**, 148 (2015).
- [14] G. Wang, L. Bouet, M. M. Glazov, T. Amand, E. L. Ivchenko, E. Palleau, X. Marie, and B. Urbaszek, *2D Mater.* **2**, 034002 (2015).
- [15] A. A. Mitioglu, P. Plochocka, A. Granados del Aguila, P. C. M. Christianen, G. Deligeorgis, S. Anghel, L. Kulyuk, and D. K. Maude, *Nano Lett.* **15**, 4387 (2015).
- [16] A. V. Stier, N. P. Wilson, K. A. Velizhanin, J. Kono, X. Xu, and S. A. Crooker, *Phys. Rev. Lett.* **120**, 057405 (2018).
- [17] M. Koperski, M. R. Molas, A. Arora, K. Nogajewski, M. Bartos, J. Wyzula, D. Vaclavkova, P. Kossacki, and M. Potemski, *2D Mater.* **6**, 015001 (2018).
- [18] X.-X. Zhang, T. Cao, Z. Lu, Y.-C. Lin, F. Zhang, Y. Wang, Z. Li, J. C. Hone, J. A. Robinson, D. Smirnov, S. G. Louie, and T. F. Heinz, *Nat. Nanotechnol.* **12**, 883 (2017).
- [19] M. R. Molas, C. Faugeras, A. O. Slobodeniuk, K. Nogajewski, M. Bartos, D. M. Basko, and M. Potemski, *2D Mater.* **4**, 021003 (2017).
- [20] C. Robert, T. Amand, F. Cadiz, D. Lagarde, E. Courtade, M. Manca, T. Taniguchi, K. Watanabe, B. Urbaszek, and X. Marie, *Phys. Rev. B* **96**, 155423 (2017).
- [21] Y. You, X.-X. Zhang, T. C. Berkelbach, M. S. Hybertsen, D. R. Reichman, and T. F. Heinz, *Nat. Phys.* **11**, 477 (2015).
- [22] M. Barbone, A. R.-P. Montblanch, D. M. Kara, C. Palacios-Berraquero, A. R. Cadore, D. De Fazio, B. Pingault, E. Mostaani, H. Li, B. Chen, K. Watanabe, T. Taniguchi, S. Tongay, G. Wang, A. C. Ferrari, and M. Atatüre, *Nat. Commun.* **9**, 3721 (2018).
- [23] A. Steinhoff, M. Florian, A. Singh, K. Tran, M. Kolarczik, S. Helmrich, A. W. Achtstein, U. Woggon, N. Owschimikow, F. Jahnke, and X. Li, *Nat. Phys.* **14**, 1199 (2018).
- [24] Z. Li, T. Wang, Z. Lu, C. Jin, Y. Chen, Y. Meng, Z. Lian, T. Taniguchi, K. Watanabe, S. Zhang, D. Smirnov, and S.-F. Shi, *Nat. Commun.* **9**, 3719 (2018).
- [25] K. F. Mak, K. He, C. Lee, G. H. Lee, J. Hone, T. F. Heinz, and J. Shan, *Nat. Mater.* **12**, 207 (2013).
- [26] E. Courtade, M. Semina, M. Manca, M. M. Glazov, C. Robert, F. Cadiz, G. Wang, T. Taniguchi, K. Watanabe, M. Pierre, W. Escoffier, E. L. Ivchenko, P. Renucci, X. Marie, T. Amand, and B. Urbaszek, *Phys. Rev. B* **96**, 085302 (2017).

- [27] Y. Zhou, G. Scuri, D. S. Wild, A. A. High, A. Dibos, L. A. Jauregui, C. Shu, K. d. Greve, K. Pistunova, A. Joe, T. Taniguchi, K. Watanabe, P. Kim, M. D. Lukin, and H. Park, *Nat. Nanotechnol.* **12**, 856 (2017).
- [28] G. Wang, C. Robert, M. M. Glazov, F. Cadiz, E. Courtade, T. Amand, D. Lagarde, T. Taniguchi, K. Watanabe, B. Urbaszek, and X. Marie, *Phys. Rev. Lett.* **119**, 047401 (2017).
- [29] E. Liu, J. van Baren, Z. Lu, M. M. Altairy, T. Taniguchi, K. Watanabe, D. Smirnov, and C. H. Lui, *Phys. Rev. Lett.* **123**, 027401 (2019).
- [30] Z. Li, T. Wang, Z. Lu, M. Khatoniar, Z. Lian, Y. Meng, M. Blei, T. Taniguchi, K. Watanabe, S. A. McGill, S. Tongay, V. M. Menon, D. Smirnov, and S.-F. Shi, *Nano Lett.* **19**, 6886 (2019).
- [31] E. Liu, J. van Baren, T. Taniguchi, K. Watanabe, Y.-C. Chang, and C. H. Lui, *Phys. Rev. Research* **1**, 032007 (2019).
- [32] M. He, P. Rivera, D. Van Tuan, N. P. Wilson, M. Yang, T. Taniguchi, K. Watanabe, J. Yan, D. G. Mandrus, H. Yu, H. Dery, W. Yao, and X. Xu, *Nat. Commun.* **11**, 618 (2020).
- [33] D. Wickramaratne, F. Zahid, and R. K. Lake, *J. Chem. Phys.* **140**, 124710 (2014).
- [34] H. Terrones and M. Terrones, *J. Mater. Res.* **29**, 373 (2014).
- [35] N. R. Wilson, P. V. Nguyen, K. Seyler, P. Rivera, A. J. Marsden, Z. P. Laker, G. C. Constantinescu, V. Kandyba, A. Barinov, N. D. M. Hine, X. Xu, and D. H. Cobden, *Sci. Adv.* **3**, 1601832 (2017).
- [36] Z. Li, T. Wang, C. Jin, Z. Lu, Z. Lian, Y. Meng, M. Blei, S. Gao, T. Taniguchi, K. Watanabe, T. Ren, S. Tongay, L. Yang, D. Smirnov, T. Cao, and S.-F. Shi, *Nat. Commun.* **10**, 2469 (2019).
- [37] D. Van Tuan, A. M. Jones, M. Yang, X. Xu, and H. Dery, *Phys. Rev. Lett.* **122**, 217401 (2019).
- [38] J. Lindlau, C. Robert, V. Funk, M. Förg, L. Colombier, A. Neumann, T. Taniguchi, K. Watanabe, M. M. Glazov, X. Marie, B. Urbaszek, and A. Högele, [arXiv:1710.00988](https://arxiv.org/abs/1710.00988) (2017).
- [39] S. Fang, R. Kuate Defo, S. N. Shirodkar, S. Lieu, G. A. Tritsarlis, and E. Kaxiras, *Phys. Rev. B* **92**, 205108 (2015).
- [40] D. V. Rybkovskiy, I. C. Gerber, and M. V. Durnev, *Phys. Rev. B* **95**, 155406 (2017).
- [41] L. D. Landau and E. M. Lifshitz, *Quantum mechanics: Non-relativistic theory*, Vol. 3 (Elsevier, 2013).
- [42] L. M. Roth, B. Lax, and S. Zwerdling, *Phys. Rev.* **114**, 90 (1959).
- [43] G. L. Bir and G. E. Pikus, *Symmetry and strain-induced effects in semiconductors* (Wiley New York, 1974).
- [44] D. Xiao, M.-C. Chang, and Q. Niu, *Rev. Mod. Phys.* **82**, 1959 (2010).
- [45] M. H. Cohen and E. I. Blount, *Philos. Mag.* **5**, 115 (1960).
- [46] M.-C. Chang and Q. Niu, *Phys. Rev. B* **53**, 7010 (1996).
- [47] G. I. Csonka, J. P. Perdew, A. Ruzsinszky, P. H. T. Philipsen, S. Lebègue, J. Paier, O. A. Vydrov, and J. G. Ángyán, *Phys. Rev. B* **79**, 155107 (2009).
- [48] S. Grimme, J. Antony, S. Ehrlich, and H. Krieg, *J. Chem. Phys.* **132**, 154104 (2010).
- [49] S. Grimme, S. Ehrlich, and L. Goerigk, *J. Comp. Chem.* **32**, 1456 (2011).
- [50] A. Arora, M. Koperski, A. Slobodeniuk, K. Nogajewski, R. Schmidt, R. Schneider, M. R. Molas, S. M. de Vasconcellos, R. Bratschitsch, and M. Potemski, *2D Mater.* **6**, 015010 (2018).
- [51] T. Deilmann and K. S. Thygesen, *2D Mater.* **6**, 035003 (2019).